INTERNATIONAL JOURNAL FOR NUMERICAL METHODS IN FLUIDS
Int. J. Numer. Meth. Fluids 2000; **33**: 869–895

Prediction of turbulent oscillatory flows in complex systems

P. G. Tucker*

School of Engineering, The University of Warwick, Coventry, U.K.

SUMMARY

The economical prediction of a turbulent oscillatory isothermal flow at transitional Reynolds numbers is considered for an enclosure representative of an idealized electronics system. To assess the accuracy of numerical models, comparison is made with measurements. Normal wall distances, required in some turbulence models, are evaluated using a modified Poisson equation-based technique. Solutions of the Poisson and fluid flow equations are accelerated using multi-level schemes, giving valuable time-savings. The Poisson equation-based wall distance technique is shown to be effective. Zero- to two-equation turbulence techniques are tested, including zonal and non-linear eddy viscosity models. Of the nine models tested, the zonal models showed greatest potential. Copyright © 2000 John Wiley & Sons, Ltd.

KEY WORDS: complex system; multilevel convergence; oscillatory; turbulence; wall distance algorithm; zonal modelling

1. INTRODUCTION

The economical prediction of complex system turbulent oscillatory flows at transitional Reynolds numbers is important for a wide range of industrial applications. These include the design of electronics enclosures and clean rooms. The former subject is reviewed by Tucker [1]. Accurate turbulence intensity and oscillatory flow component predictions are important for the modelling of both contaminant and heat transport. For electronic systems, the Reynolds number (Re) range is typically $100 < Re < 5000$ and the geometry is generally complex with many corners, recesses and boundary layer and flow stagnation surfaces. Reynolds numbers can vary significantly in different regions of a single system. All the above make the potential for the excitement of an oscillatory turbulent flow relatively high.

* Correspondence to: School of Engineering, The University of Warwick, Coventry, CV4 7AL, U.K.

Received July 1999
Revised September 1999

Using a semi-analytical technique, Rockwell [2] predicted oscillation frequencies for flow over a rectangular cavity. Rockwell and Naudascher [3] proposed that oscillatory flows are caused by shear layer instabilities with impingement. Evidently, feedback from the impingement region maintains the oscillations. For three-dimensional flows, this feedback mechanism is complex. The possibility of oscillatory flow is a function of viscosity [4]. This suggests that for turbulent eddy viscosity-based predictions, oscillatory behaviour will be sensitive to effective viscosity levels.

Ghaddar *et al*. [5] numerically studied two-dimensional isothermal laminar flow in channels with rectangular blocks using a spectral element method. For $Re > 1000$ (based on the channel half-width), a complex oscillatory flow is found. Ghaddar *et al*. [6] and Patera and Mikic [7] made predictions illustrating the increased heat transport caused by the oscillatory nature of the flow. Nigen and Amon [8–10] extended the above to include realistic electronic component thermal modelling. The modelling of differentially heated cavity laminar oscillatory flows has also been addressed by Pulicani *et al*. [11]. Rockwell [12] presented particle image velocimetry data for turbulent oscillatory flow over a cavity. Large-scale vortex structures associated with the oscillatory flow component are observed.

There has been little consideration of the economical prediction of forced convection turbulent oscillatory flows in complex engineering systems. This will be addressed here for the geometry shown in Figure 1, which is representative of an electronic system. The geometry consists of three main hollow block-like components, defined as regions 1, 2 and 3. Regions 1 and 2 have fans attached to them. To assess the accuracy of the numerical models, comparison is made with Pitot static tube and hot wire anemometry velocity data and also hot wire anemometry turbulence intensity data [13]. Although the flow is unsteady, this component has not been removed from the turbulence intensity data. Instead, predictions are corrected, enabling direct comparisons.

Electronic system geometries often have many (several hundred for a complex system) surfaces. Distances from these are required in some turbulence models. Rather than use crude search procedures, a modified differential equation-related distance algorithm based on that developed by Spalding [14] is tried. The numerous surfaces produce many channel-like regions. In these, simpler turbulence models may give reasonable predictions. Motivated by this idea and the computational expense of accurately resolving gradients in every channel, Spalding developed the zero-equation l–v (or L–Vel in the original paper) model. In this, the turbulent viscosity is established by differentiating a single-equation law of the wall [15]. The l–v model is tested here. For interest, comparison is also made with a mixing length model.

Improvements by solving for turbulent kinetic energy, k, transport in high- and low- [16] Reynolds number k–l models is then considered. For certain systems, these models may provide a reasonable compromise between accuracy and computational economy. The high-Reynolds number k–ε [17] model is popular in electronic systems design and here its performance is further assessed. To study the importance of accounting for anisotropy, a high-Reynolds number, non-linear eddy viscosity model [18] is also tried. With wall functions, the low Reynolds numbers in electronic systems and clean rooms make it difficult to ensure first-off wall grid nodes are not too near walls. However, without them the k–ε model requires computationally expensive fine near-wall grids. These considerations make zonal turbulence

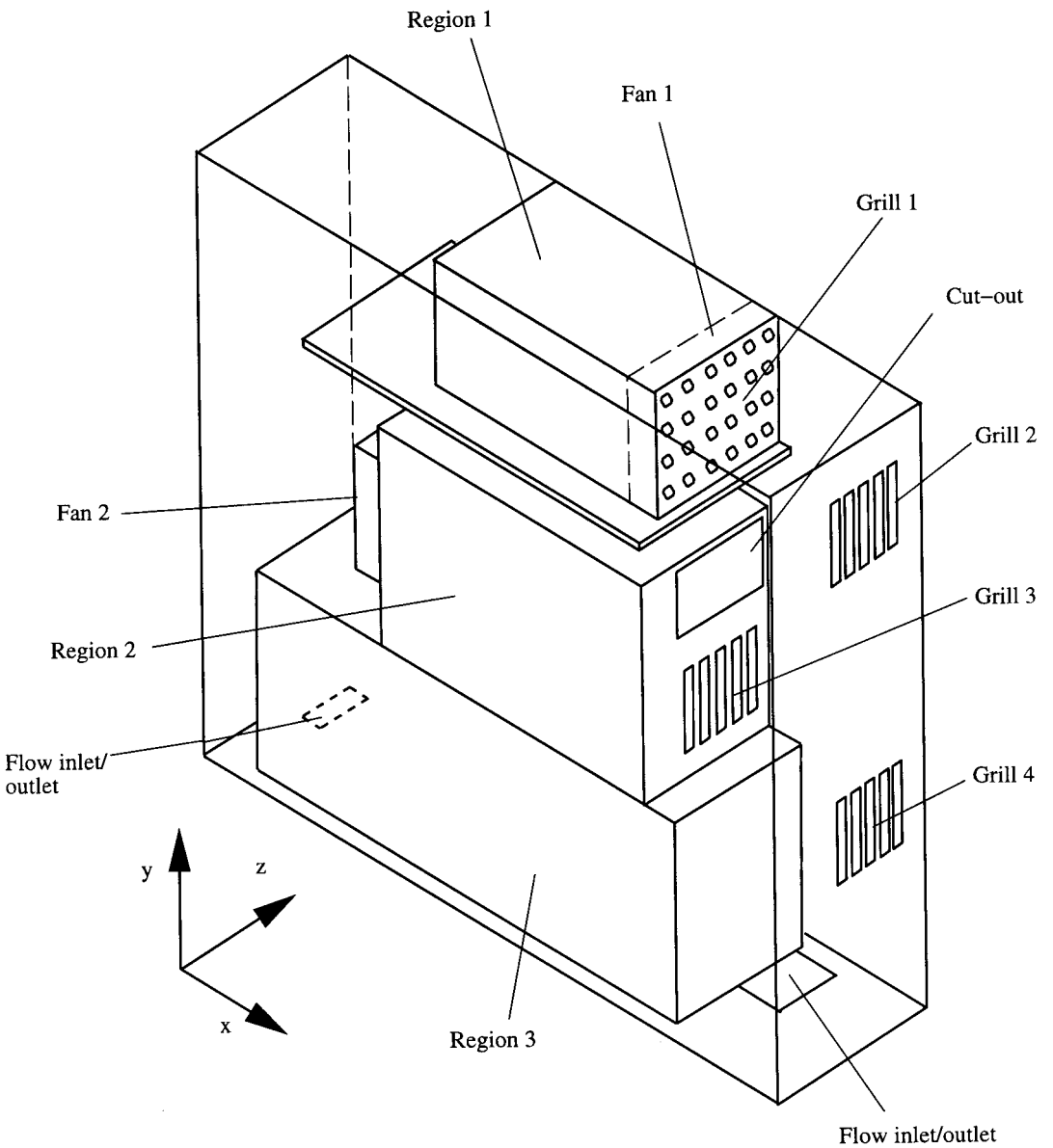

Figure 1. Schematic of system to be considered.

models attractive. The technique has been used by Iacovides and Theofanopoulos [19] and Iacovides and Chew [20] for rotating flows related to aero engine cavities. It is also applied here. In the present work, away from walls, the $k-\varepsilon$ model is used. Near walls, two different

mixing length models and a k–l treatment are compared. The models used are summarized below.

I. standard Van Driest damping function-based mixing length model (ml_1)
II. the single-equation law of the wall-based (l–v) model
III. a high-Reynolds number k–l model (k–l_1)
IV. the low-Reynolds number k–l model [16] (k–l_2)
V. the standard k–ε model
VI. a zonal turbulence technique with the k–l_2 model (k–ε/k–l_2)
VII. a zonal turbulence technique with the ml_1 model (k–ε/ml_1)
IX. the above with a more refined damping function in the ml_1 model (k–ε/ml_2)
X. a non-linear eddy viscosity model (nl–k–l_1)

2. NUMERICAL METHOD

2.1. Key governing equations

Conservation of momentum for the system considered here can be expressed in the following tensor form:

$$\frac{\partial U_i}{\partial t}+\frac{\partial U_i U_j}{\partial x_j}=-\frac{1}{\rho}\frac{\partial p}{\partial x_i}+\frac{\mu}{\rho}\frac{\partial}{\partial x_j}\left(\frac{\partial U_i}{\partial x_j}+\frac{\partial U_j}{\partial x_i}\right)+\frac{\partial(-\overline{u_i' u_j'})}{\partial x_j} \tag{1}$$

where U is the mean fluid velocity component, $\overline{u'}$ is the averaged fluctuating component, ρ is the fluid density, μ is the viscosity, p is the static pressure, t is the time, and x is the spatial co-ordinate. The corresponding continuity equation is

$$\frac{\partial U_j}{\partial x_j}=0 \tag{2}$$

Unless otherwise stated, to approximate the Reynolds stress related terms, the Boussinesq approximation is used in the following form:

$$-\overline{u_i' u_j'}=-n_0\frac{2}{3}k\delta_{ij}+\frac{2\mu_t}{\rho}S_{ij} \tag{3}$$

where δ_{ij} is the Kronecker delta ($\delta_{ij}=1$ if $i=j$ and $\delta_{ij}=0$ if $i\neq j$), μ_t is the turbulent viscosity, k is the turbulent kinetic energy, and $n_0=0$ or 1 depending on the model used. The term S_{ij} (the mean strain rate) has the following form:

$$S_{ij} = \frac{1}{2}\left(\frac{\partial U_i}{\partial x_j} + \frac{\partial U_j}{\partial x_i}\right) \tag{4}$$

When k is required, the following differential transport equation is used:

$$\frac{\partial \phi}{\partial t} + \frac{\partial U_j \phi}{\partial x_j} = \frac{1}{\rho}\frac{\partial}{\partial x_j}\left(\Gamma_\phi \frac{\partial \phi}{\partial x_j}\right) - T_1 \overline{u_i' u_j'} \frac{\partial U_i}{\partial x_j} - T_2 \tag{5}$$

where $\phi = k$, $\Gamma_k = \mu + \mu_t/\sigma_k$ (where σ_k is the diffusion Prandtl number for k), $T_1 = 1$ and $T_2 = \varepsilon$ (the rate of dissipation of turbulence kinetic energy). When $\phi = \varepsilon$, $\Gamma_\varepsilon = \mu + \mu_t/\sigma_\varepsilon$ (where σ_ε is the diffusion Prandtl number for ε), $T_1 = C_{\varepsilon 1}\,\varepsilon/k$, and $T_2 = C_{\varepsilon 2}\,\varepsilon^2/k$, Equation (5) can also be used to estimate the rate of dissipation of k. For some modelling approaches, the rate of dissipation can also be related to the normal distance from walls, y, and so this is an important parameter to evaluate.

2.2. Calculation of normal wall distances

For complex cluttered geometries, y can be calculated using a method derived by Spalding [14] (a detailed presentation of this is given by Tucker [21]). This involves the solution of a Poisson equation of the following form:

$$\frac{\partial}{\partial x_j}\left(\frac{\partial L}{\partial x_j}\right) = C \tag{6}$$

where $C = -1$, and at solid walls $L = 0$, otherwise the condition $\partial L/\partial y = 0$ is used. Unlike when nearest wall search procedures are used, at corners this method produces smooth variations in y, and hence μ_t. This can help convergence. Here, y is related to L using the slightly modified (absolute values of gradients are used) expression to Spalding's derived by Tucker [21] and given below

$$y = -\sum_{j=1,3}\left|\frac{\partial L}{\partial x_j}\right| \pm \sqrt{\left(\sum_{j=1,3}\left|\frac{\partial L}{\partial x_j}\right|\right)^2 + 2L} \tag{7}$$

Derivation of the above requires the assumption that the surface perpendicular to y is infinite. This approximation is reasonable in the regions of importance, which are close to surfaces. Equation (7) has negative and positive roots corresponding to nearest ($y_{\min}$) and furthest ($y_{\max}$) normal wall distances. Therefore, the approximate distance between two surfaces is equal to $y_{\min} + y_{\max}$. Solutions of the Poisson and fluid flow equations are accelerated using the multi-level scheme described later.

An alternative to the Poisson equation-based algorithm above would be the fast marching methods of Sethian [22]. For wall distances, these involve the solution of the generic equation $|\nabla L| = 1$. However, since for this equation L is not continuous in corners (where there can be two nearest wall distances), a small diffusion term is added to the right-hand side (if not small this constitutes an error). This gives an essentially convection–diffusion-type equation, which can be solved by marching from boundaries. The technique has the advantage that it can also

accurately find distances between surfaces. This is useful when evaluating things such as radiative exchange factors in heat transfer problems. However, for standard Navier–Stokes equation solvers, relative to the Poisson equation technique, its implementation does not appear to be as natural.

In this paper, nine turbulence models are tested. These are briefly described below in the approximate order of complexity/accuracy.

I. Standard mixing length model

For this (ml_1) model

$$\mu_t = \rho l_\mu^2 \left[2 \frac{\partial U_i}{\partial x_j} S_{ij} \right]^{1/2} \tag{8}$$

where l_μ is a mixing length. In the near-wall region, the original Van Driest damping function is used, giving

$$l_\mu = \kappa y \left(1 - \exp \frac{-y^+}{26} \right) \tag{9}$$

where y^+ is the dimensionless wall distance equal to $(\rho \tau_w)^{1/2} y/\mu$, τ_w is the wall shear stress and κ the von Karman constant. The modified function [23] below

$$l_\mu = \kappa y \left(1 - \exp \frac{-(\tau/\tau_w)^{1.5} y^+}{26} \right) \tag{10}$$

is also tried. Equation (10) (for the ml_2 model) is only used for the zonal model to be described later. Outside the near-wall region

$$l_\mu = \kappa \delta \tag{11}$$

where δ is an approximation to the boundary layer thickness. The normal wall distance is again calculated using the novel Poisson equation procedure, where $y = y_{\min}$ in the mixing length equations. The above are used with $n_0 = 0$ in Equation (3).

II. l–v Model

The basis for this model is Spalding's [15] single-equation, Taylor series-based law of the wall

$$y^+ = u^+ + \frac{1}{E} \left[e^{\kappa u^+} - 1 - \frac{\kappa u^+}{1!} - \frac{(\kappa u^+)^2}{2!} - \frac{(\kappa u^+)^3}{3!} - \frac{(\kappa u^+)^4}{4!} \right] \tag{12}$$

This can be differentiated to give the dimensionless effective viscosity. This differentiated result can then be rearranged to yield the following effective viscosity expression:

$$\mu_t = \mu \frac{\kappa}{E}\left[e^{\kappa u^+} - 1 - \frac{\kappa u^+}{1!} - \frac{(\kappa u^+)^2}{2!} - \frac{(\kappa u^+)^3}{3!} \right] \tag{13}$$

The dimensionless velocity $u^+ = U(\rho/\tau_w)^{1/2}$ in Equation (13) is calculated using a Newton–Raphson procedure needing y. As recommended by Spalding [14], y is computed with Equation (7). In Equation (3), $n_0 = 0$.

III and IV. k–l Models

Equation (4) is solved for $\phi = k$, and ε defined using

$$\varepsilon = \frac{k^{3/2}}{l_\varepsilon} \tag{14}$$

where

$$l_\varepsilon = C_{\varepsilon 0} y \left(1 - n_1 \exp \frac{-A_\varepsilon y^+}{C_\mu^{1/4}} \right) \tag{15}$$

and $y^+ = y\rho k^{1/2} C_\mu^{1/4}/\mu$. The turbulent viscosity can be expressed as

$$\mu_t = \rho C_\mu l_\mu k^{1/2} \tag{16}$$

where

$$l_\mu = C_{\mu 0} y \left[1 - n_1 \exp\left(-\frac{A_\mu y^+}{C_\mu^{1/4}} \right) \right] \tag{17}$$

When $n_1 = 1$, the length scales l_ε and l_μ have near-wall damping functions and the model (k–l_2) is as described by Wolfshtein [16]. For comparison, predictions are also made with $n_1 = 0$ and computationally economical logarithmic wall functions [17]. The implementation of these is noted later. This high-Reynolds number model is called here the k–l_1 model.

V. k–ε Model

For this, Equation (5) is solved with $\phi = k$ and ε, and the turbulent viscosity found using

$$\mu_t = \rho C_\mu \frac{k^2}{\varepsilon} \tag{18}$$

The model is standard [17] using logarithmic wall functions.

VI, VII and VIII. Zonal models

In this approach, for $y^+ \geq 60$, the k–ε method is used and for $y^+ < 60$, the k–l_2, ml_1 or ml_2 models are applied. To connect these differing models at the $y^+ = 60$ interface, patching conditions are needed. For the k–ε/k–l_2 method (model VI), Equation (19)

$$k^{3/2} = l_\mu \varepsilon \tag{19}$$

is used (rearranged for ε). For the k–ε/ml_1 and k–ε/ml_2 methods (models VII and VIII respectively), the following additional condition is needed:

$$\varepsilon = -\overline{u_i' u_j'} \frac{\partial U_i}{\partial x_j} \tag{20}$$

IX. High-Reynolds number non-linear eddy viscosity model

This model (nl–k–l_1) is based on Speziale's model [18]. It essentially involves using the quadratic 'Boussinesq' approximation

$$-\overline{u_i' u_j'} = -\frac{2}{3} k\delta_{ij} + 2\frac{\mu_t}{\rho} S_{ij} + 4C_D C_\mu \frac{\mu_t}{\rho}\frac{k}{\varepsilon}\left(S_{ik}S_{kj} - \frac{1}{3} S_{mn}S_{nm}\delta_{ij}\right) + 4C_E C_\mu \frac{\mu_t}{\rho}\frac{k}{\varepsilon}\left(\mathring{S}_{ij} - \frac{1}{3}\mathring{S}_{mm}\delta_{ij}\right) \tag{21}$$

The $\mathring{S}_{ij}$ term is called the Oldroyd derivative, which can be expressed as

$$\mathring{S}_{i,j} = \frac{\partial S_{ij}}{\partial t} + U_k \frac{\partial S_{ij}}{\partial x_k} - \frac{\partial U_i}{\partial x_k} S_{kj} - \frac{\partial U_j}{\partial x_k} S_{ki} \tag{22}$$

Here the model is incorporated in a k–l framework, with Equation (21) replacing Equation (3) in the linear k–l_1 model. Non-linear contributions from Equation (21) are differentiated and then directly incorporated into the momentum equations. Following Speziale, velocities in the non-linear part of the 'Boussinesq' approximation are smoothed. Here, for convenience, this is done using the restriction operators (essentially consisting of an 18-point distance weighted averaging) from the multi-level algorithm described later.

The following standard constants are used in the above models: $\sigma_k = 1$, $\sigma_\varepsilon = 1.3$, $A_\varepsilon = 0.263$, $A_\mu = 0.016$, $C_E = C_D = 1.68$, $C_{\varepsilon 0} = 2.4$, $C_{\varepsilon 1} = 1.44$, $C_{\varepsilon 2} = 1.92$, $C_{\mu 0} = 2.4$, $C_\mu = 0.09$, $\kappa = 0.41$, $E \approx 9.0$.

2.3. General program features

The governing equations are discretized using a standard structured staggered grid technique [24]. In results, the upwind and second-order central difference based CONDIF [25] convective term treatments are compared. Diffusion terms are discretized in a second-order manner. The pressure field is computed using the SIMPLE [26] method. For transient predictions, a fully implicit time scheme is used. Rather than use high viscosities to define solid regions, a Boolean marker array [n] is used. At fluid, solid and differential boundary condition regions, individual entries of n take the following, respective, values 1, 0, -1. This marker array technique requires extra storage. However, for non-conjugate problems, it prevents wasted computations on redundant cells and, importantly, easily allows second-order wall treatments.

2.4. Multilevel algorithm

Standard iterative methods are inefficient at reducing low frequency errors with wavelengths greater than the grid spacing. The multi-level technique outlined below enhances the reduction of these errors by using coarser grids. The method is described by Brandt [27]. In a SIMPLE framework there are many examples of its application. For example, Lonsdale [28] and Vaughan *et al.* [29] apply the technique to laminar and turbulent rectangular rotating cavity flows respectively. Also, Rayner [30,31] and Shy *et al.* [32,33] use multi-level convergence for solutions involving body-fitted co-ordinate systems. Thompson and Ferziger [34] illustrate the methods potential in adaptive grid frameworks. Raw [35] presents a linear multi-level method, suitable for unstructured grids. For completeness, the new three-dimensional implementation in the present code is briefly outlined. The equation sets to be solved can be expressed as

$$[A_m][\phi_m] = [S_m] \tag{23}$$

where $[\phi_m]$, $[A_m]$ and $[S_m]$ are the solution, discretized equation coefficient and source term arrays respectively. The subscript m indicates the current grid level with $m = 1$ referring to the finest grid. If it is assumed that the solution can be expressed as the sum of approximate values $[\phi_m^{\mathrm{a}}]$ and corrections $[\phi_m^{\mathrm{c}}]$ to these, Equation (23) can be stated as

$$[A_m][\phi_m^{\mathrm{a}} + \phi_m^{\mathrm{c}}] = [R_m] + [A_m][\phi_m^{\mathrm{a}}] \tag{24}$$

where $[R_m] = [S_m] - [A_m][\phi_m^{\mathrm{a}}]$ is the residual error. For a coarser mesh, denoted by $m+1$, Equation (24) can be rewritten as

$$[A_{m+1}][\phi_{m+1}^{\mathrm{a,f}} + \phi_{m+1}^{\mathrm{c}}] = [R_m^{\mathrm{f}}] + [A_{m+1}][\phi_{m+1}^{\mathrm{a,f}}] \tag{25}$$

where the superscript f indicates values originating from a finer mesh. Equation (25) solves for the full approximation $\phi_{m+1}^{\mathrm{a,f}} + \phi_{m+1}^{\mathrm{c}}$ (a full approximation storage scheme). Corrections for lower grid levels can be obtained by subtracting $\phi_m^{\mathrm{a,f}}$ from the full approximation. For $\phi = L$, $[A_{m+1}][\phi_{m+1}^{\mathrm{a,f}} \cdots]$ cancels in Equation (25) and the linear correction storage equation

$$[A_{m+1}][\phi_{m+1}^{\mathrm{c}}] = [R_{m+1}^{\mathrm{f}}] \tag{26}$$

can be used. For a two grid method, ϕ_{m+1}^{c} is interpolated to grid level m where

$$[\phi_m] = [\phi_m^{\mathrm{a,f}}] + \alpha[\phi_{m+1}^{\mathrm{c}}] \tag{27}$$

and α is an under- or overrelaxation parameter. Importantly, a correction equation on grid level $m+2$ could be written for Equations (25) and (26) themselves (which have essentially the same form as Equation (23)). This procedure could be repeated on higher grid levels, until no further coarsening can take place. This is the basis of the multi-level method, which is incorporated here in a fixed V-cycle, the solution starting with $m = 1$, progressing to higher levels and then returning to $m = 1$. Here, the method is applied to the coupled set of flow

equations as an outer iteration to the SIMPLE method. For complex geometries, when $m > 2$, it is impractical to prevent geometrical distortion [36]. Therefore, a maximum of three grid levels are used. Importantly, even for $m = 2$, no attempt is made to prevent distortion by fixing grid lines adjacent to solid surfaces. Despite this [21], the multi-level method can still produce worthwhile savings. If the grid distortion does prevent convergence to the desired level, some final single grid iterations can be used and time savings still be made.

To represent variables on, say, level $m+1$ from level m (a process called restriction), a 27-point distance weighted averaging is used for main grid point variables. For staggered variables, 18 points are used. Once corrections (ϕ^{c}_{m+1}) have been calculated, they are bilinearly interpolated (prolongated) onto the next finer grid level. As noted by Tucker [37] and others, the turbulence equations can sometimes show poor multi-level convergence. Therefore, here they are solved for $m = 1$. Turbulence values required at $m > 1$ are restricted. Simultaneous equation sets are solved using a tridiagonal matrix algorithm. Underrelaxation is carried out implicitly through the coefficients of the discretized equations.

2.5. Evaluation of turbulence intensities

The turbulent flow to be studied is unsteady. Consequently, the measured instantaneous resolved velocity $q = \sqrt{u^2 + v^2 + w^2}$ is the sum of Q (the time averaged velocity) and fluctuations due to turbulence q' and unsteadiness q''

$$q = Q + q' + q'' \tag{28}$$

Measurements of turbulence intensity to be compared with have not been corrected for the effect of flow unsteadiness. These intensities can be expressed as

$$T'_i = \frac{1}{Q_0}\sqrt{(q-Q)^2} \tag{29}$$

To enable comparisons with measurements, T'_i is evaluated stochastically by expressing

$$q = Q + N\sqrt{\frac{2}{3}k} + q'' \tag{30}$$

where N is a Gaussian random number with a standard deviation of unity and $\overline{q'^2} = 2k/3$. Following Gosman and Ioannides [38], the concept of an eddy is used. The size of these eddies is approximated by the dissipation length scale

$$l = C_\mu^{3/4}\frac{k^{3/2}}{\varepsilon} \tag{31}$$

An eddy lifetime is defined as

$$t_e = \frac{l}{q'} \tag{32}$$

along with the approximate time for an eddy to traverse a measurement probe

$$t_p = \frac{l}{q} \tag{33}$$

It then follows that the maximum eddy/probe interaction time Δt_{max} is given by

$$\Delta t_{max} = \min(t_e, t_p) \tag{34}$$

To approximate the nature of the measured turbulence and hence numerically evaluate T_i', N is recomputed at intervals of $\Delta t_{max} = \min(t_e, t_p)$. In the context of the present paper, since $\overline{q'q''} = 0$, the use of the above procedure can be avoided. However, it has potential use when estimating other turbulence related parameters.

2.6. Boundary conditions

For velocities at solid surfaces, the usual no-slip and impermeability conditions are applied. At inflow boundaries, the total pressure is fixed, the normal velocity set to conserve mass and the remaining velocity components made zero. At flow outlets, the pressure is fixed, the normal velocity is again set to conserve mass and the gradients of all other variables set to zero in a second-order fashion. Prior to the solution starting it is not known which are inflow and outflow boundaries. Therefore, the above boundary conditions are set automatically depending on the flow direction at each iteration.

When wall functions are implemented, the diffusion of turbulence kinetic energy at walls is set to zero. Also, at first, off-wall grid nodes $\varepsilon = C_\mu k^{3/2}/\kappa y$ and when $y^+ < 11.5$, $\mu_t = 0$, otherwise $\mu_t = \mu(\kappa y^+/\ln Ey^+ - 1)$. The sensitivity of predictions to assumed values of T_i at flow inlets is tested by varying T_i between 0 and 10 per cent. Profiles presented are found insensitive to this variation.

The slotted grills 1–4 are modelled using loss coefficients of the form

$$E_l = \frac{1}{2} K \rho U_j^2 \tag{35}$$

where E_l is the loss of energy per unit volume of fluid with a local (not the lower approach velocity) velocity U_j passing through the grill. For grill 1, $K = 2$ and for the others, $K = 1$. These are reasonable K values [39]. As a sensitivity check, for grills 2–4, K is doubled and found to have no significant effect on the conclusions to be drawn here.

Fans 1 and 2 are modelled using quadratic momentum sources of the following form:

$$E_i = C_0 + C_1 U_j + C_2 U_j^2 \tag{36}$$

Table I. Fan constants.

	C_0 (J m^{-3})	C_1 (J s m^{-4})	C_2 (J s^2 m^{-5})
Fan 1	59	−12	1.1
Fan 2	59.5	−12.5	1

where E_i is the energy input per unit volume, U_j is the local normal velocity and the constants C_0, C_1 and C_2 are given in Table I.

These constants are calculated by making least-square fits to the manufacturer's data. For fan 1, measurements are made for an input voltage of 15 V. However, data is only available for inputs of 12 and 13.8 V. Therefore, linear extrapolation is used. Fan 2 is 50 per cent obstructed. To account for this, based on tests carried out by the fan manufacturer, a loss coefficient of $K = 1$ is used.

2.7. Structure of grids

Low-Reynolds number turbulence model predictions are made using a base grid with at least $105 \times 97 \times 51$ non-uniform control volumes in the x-, y- and z-directions respectively. For high-Reynolds number model predictions a mostly uniform $101 \times 89 \times 45$ grid is used. To study grid independence, a $209 \times 193 \times 101$ grid is implemented. There are nearly 30 separate boundary layer surfaces in the y- and z-directions, and 20 in the x-direction. For low-Reynolds number predictions, producing a grid that resolves the laminar sub-layers at all these surfaces and has reasonably smooth control volume width changes, and is not excessive in size, is challenging. Therefore, here control volumes are only refined adjacent to surfaces that have an area greater than around 25 per cent of the total system surface area in the plane considered or are related to flow inlet/outlet boundaries. The typical form of the grids used for low-Reynolds number predictions is illustrated for the finest $209 \times 193 \times 101$ grid (Figure 2). The views shown are at $Z = 0.5$ and $X = 0.5$, Z and X being dimensionless distances between 0 and 1 in the z- and x-directions respectively. For the zonal technique, the k–ε model is only solved when $y^+ \geq 60$. Figure 3 illustrates, using a coarser grid, node points with $y^+ \geq 60$ at $Z = 0.5$ and $X = 0.5$. For high-Reynolds number turbulence model predictions grid generation is straightforward, only requiring that adequate nodes are placed in the different 'channel' regions (produced by the many surfaces) to resolve core flows. For the grids described, at first off-wall nodes y^+_{ave} are around 2 and 15 for the low- and high-Reynolds number turbulence models respectively. Coarser multi-level algorithm grids are produced by leaving out alternate nodes.

2.8. Numerical parameters

For unsteady predictions, time steps of $\Delta t = 0.001$ s are used. To ensure convergence, conservative underrelaxation parameters of around 0.3 are set for all equations except the pressure equation where a value of 0.5 is used. For the fluid flow equations, the multi-level correction underrelaxation parameter is set at 0.3. Doubtless higher relaxation parameter values could be implemented and no attempt is made here to optimize values. For each

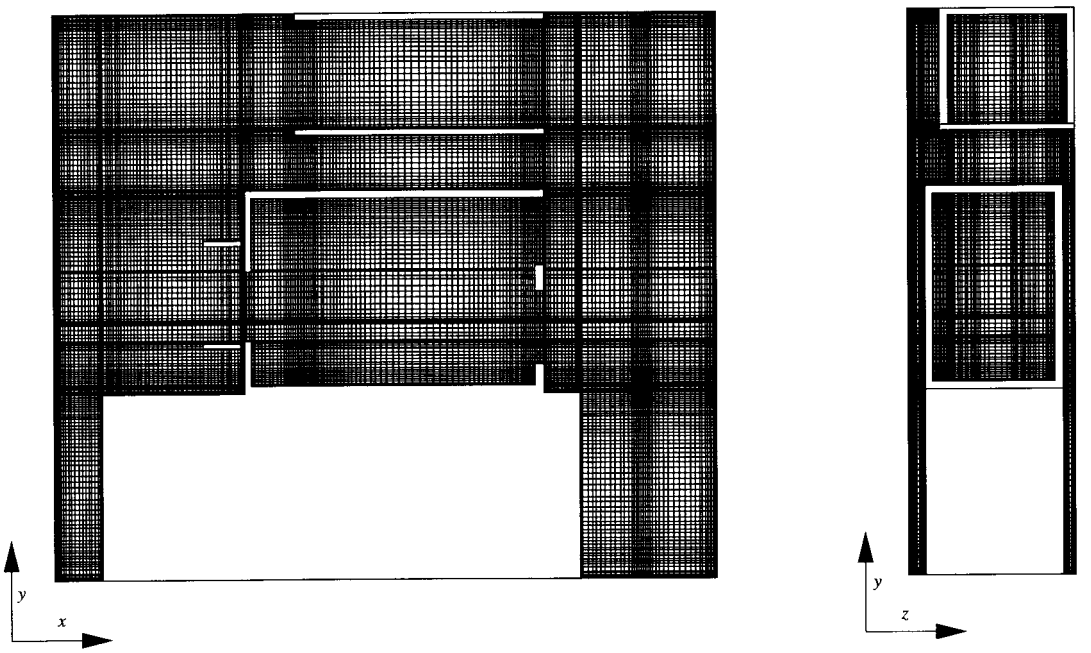

Figure 2. Typical form of grid used for low-Reynolds number predictions.

iteration six solution sweeps of the pressure correcting equation are made. For the multi-level algorithm, to minimize geometrical distortion on coarser grids, a maximum of three levels are used. Two iterations are performed on the finest grid, three on intermediate and seven on the coarsest. The fluid density and viscosity are $\rho = 1.2\ \mathrm{kg\,m^{-3}}$ and $\mu = 0.183 \times 10^{-4}\ \mathrm{kg\,m^{-1}\,s^{-1}}$ respectively.

Coarser grid predictions required around 45 Mbytes of core memory. The corresponding single grid central processor unit (CPU) time for the fluid flow and wall distance equations is 0.98 min and 5.3 s respectively. Multi-level iterations needed 3.74 min and 22 s for the flow and wall distance equations respectively. These times correspond to a 120 MHz Indigo 2 Impact 1000 computer. For the grid independence study, a 300 MHz DEC Super Scalar machine is used. This prediction required around 605 Mbytes of core memory.

Solutions are considered converged when the average normalized residual sum for the equations is less than 0.5 per cent. This loose convergence criterion is tested by comparing profiles presented here with those for residuals of an order of magnitude lower or more. No significant differences in plotted curves are observed. Moreover, the selected convergence criterion is considered compatible with the other modelling uncertainties discussed.

For profiles where predictions and measurements are compared, percentage root-mean-square (r.m.s.) errors are given. For each profile the following summation is made:

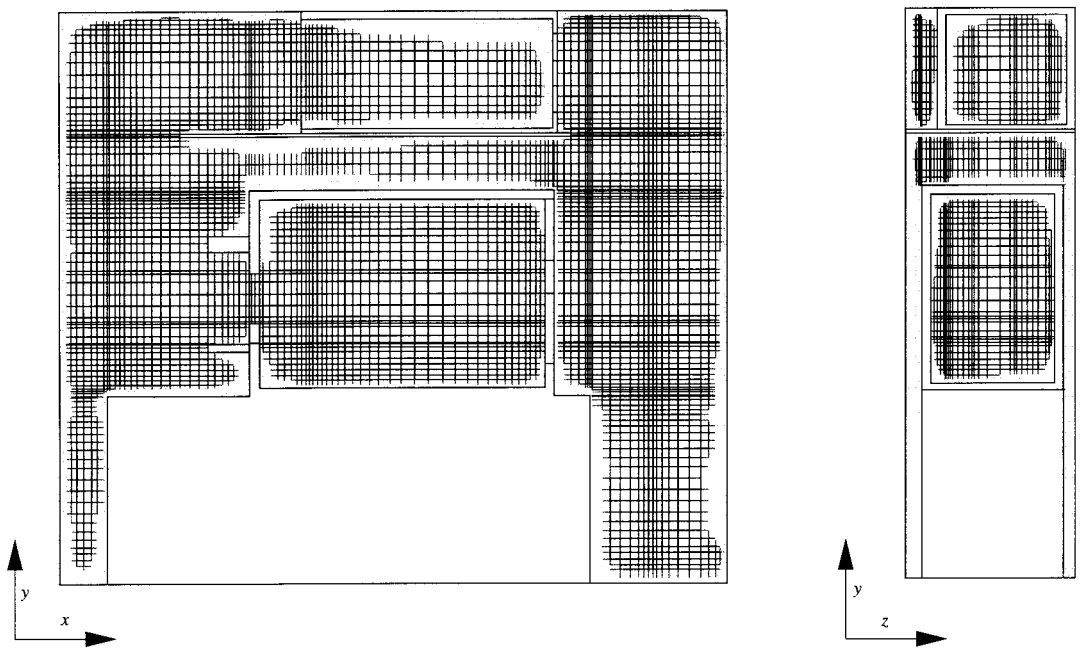

Figure 3. Diagram indicating nodes where a two-equation model is used in zonal solutions.

$$\text{Error} = \sqrt{\frac{\sum_{\text{exp}} (\phi_{\text{exp}} - \phi_{\text{num}})^2}{\sum_{\text{exp}} \phi_{\text{exp}}^2}} \tag{37}$$

where ϕ_{exp} corresponds to an experimental data point and ϕ_{num} to a numerical value. At points where numerical data points do not coincide exactly with measurements (this is mostly the case), a Bessel (stiff quadratic spline) interpolation is used.

3. DISCUSSION OF RESULTS

3.1. Multi-level convergence

Figure 4 compares the drop in mass residual against number of iterations for single level and full approximation storage, multi-level convergence. The diffusive upwind scheme and the k–l_1 model are used with a $101 \times 89 \times 45$ base grid, having three levels. Multi-level convergence about halves the CPU time. Geometry changes, for $m > 1$, stop the mass residual from going much below 3×10^{-4} kg s^{-1}. Therefore, at this value, the solution is switched to a single level. Figure 4 shows the convergence path is relatively smooth during this switch. Linear correction

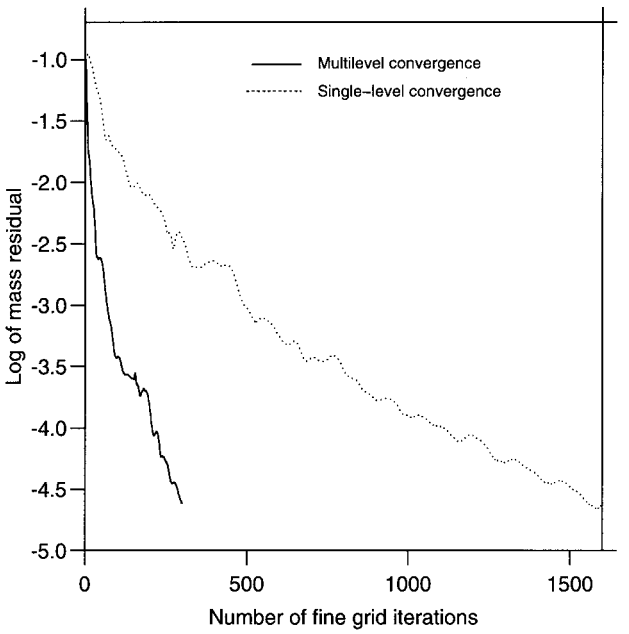

Figure 4. Multi-level convergence acceleration when using the k–l_1 turbulence model.

storage multi-level convergence is used in the solution of Equation (6), for wall distances. This gives a factor of 6.5 saving in CPU time.

Unless otherwise stated, for the remaining predictions, the less diffusive CONDIF scheme is used. Generally, this yields unsteady solutions. When Δt is small enough for time step independence, relative to single grid solutions, multi-level convergence can become inefficient. Here, it is then used to give good starting conditions, the time integration being made on a single grid. However, for the grid independence study, large time steps ($\Delta t \approx 0.1$ s) and multi-level convergence, with the k–l_2 model, proved essential—CPU time awarded on a DEC Super Scalar machine was limited to around 200 h. For each time step, multi-level convergence about halves the CPU time. For this relatively low Reynolds number flow it is expected that the conservative time steps chosen ($\Delta t = 0.001$ s) are much smaller than required for time step independence. Their relatively small size is selected to ensure both high accuracy and stability for the wide range of turbulence models tested. From experiments, the unsteady flow component, to be resolved has a period of around 2 s and the time steps chosen are 2000 times smaller than this. Average cell Courant numbers ($U_i \Delta t / \Delta x_i$) are typically less than 8×10^{-4} for high-Reynolds number turbulence model predictions and 1×10^{-2} for the more refined grid low-Reynolds number model predictions. For the k–l_1 model sensible time step independence is confirmed by switching to the higher-order Crank–Nicolson scheme time profiles for the resolved unsteady flow component exactly overlaying. A key aspect of this paper is the illustration of the drastically different turbulence intensities returned by the various turbulence

models. It is shown (Figure 10) that, as with most unsteady Reynolds-averaged Navier–Stokes solutions, these in turn greatly effect the predicted temporal behaviour, swamping if they were present any time truncation errors. The average change in turbulence intensity error values (to be presented later) for the second-order fine and coarse grid k–l_2 model predictions is less than 2.5 per cent. This gives confidence that the results presented are also sensibly grid-independent, the spatial truncation errors playing no significant part in the points the points to be made.

3.2. Wall distance algorithm

Figure 5 shows wall distance contours around the mid x–y and z–y planes. These are estimated using Equation (7). Near walls, distance variable, L, gradients are steeper and contour lines become closer. Correctly, contours are parallel to solid walls. Also, at corners, distance variations are smooth. This can be beneficial to convergence. In the important regions, close to surfaces and away from corners, distances are accurate to within 1 per cent.

3.3. Some flow features

Figure 6 is a plot of instantaneous weightless particle paths for the k–ε/k–l_2 model. Particles are seeded at the mid x–y (Figure 6(a)) and x–z (Figure 6(b)) planes. Figure 6(a) shows two recirculations downstream of fan 2 (see Figure 1). Both figures display streamline curvature and relatively large vortex structures in several regions. Vortex sizes appear limited by the enclosure boundaries. The flow features are similar for all models.

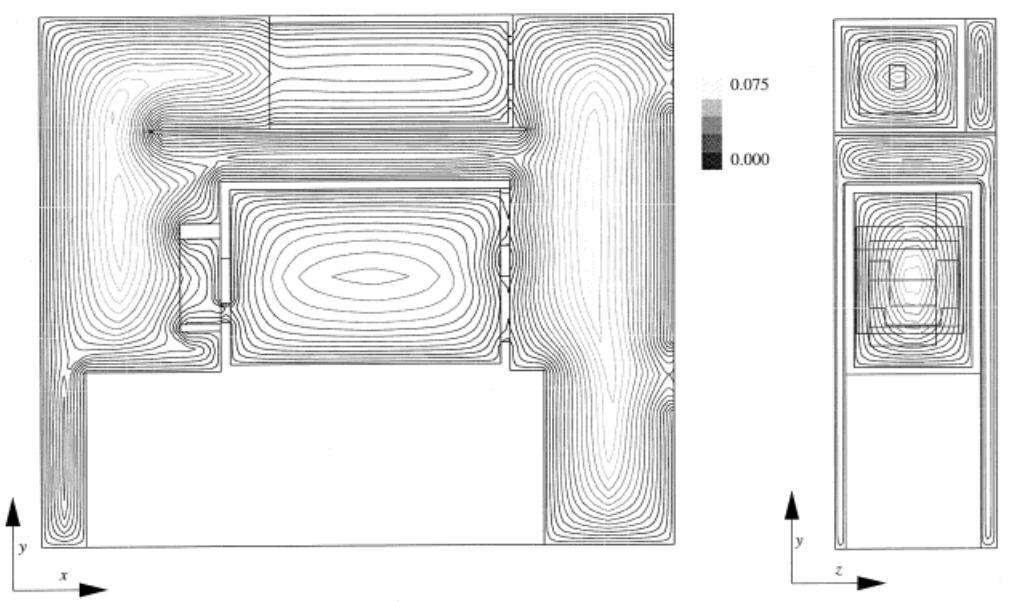

Figure 5. Wall distance contours around the mid x–y and z–y plane.

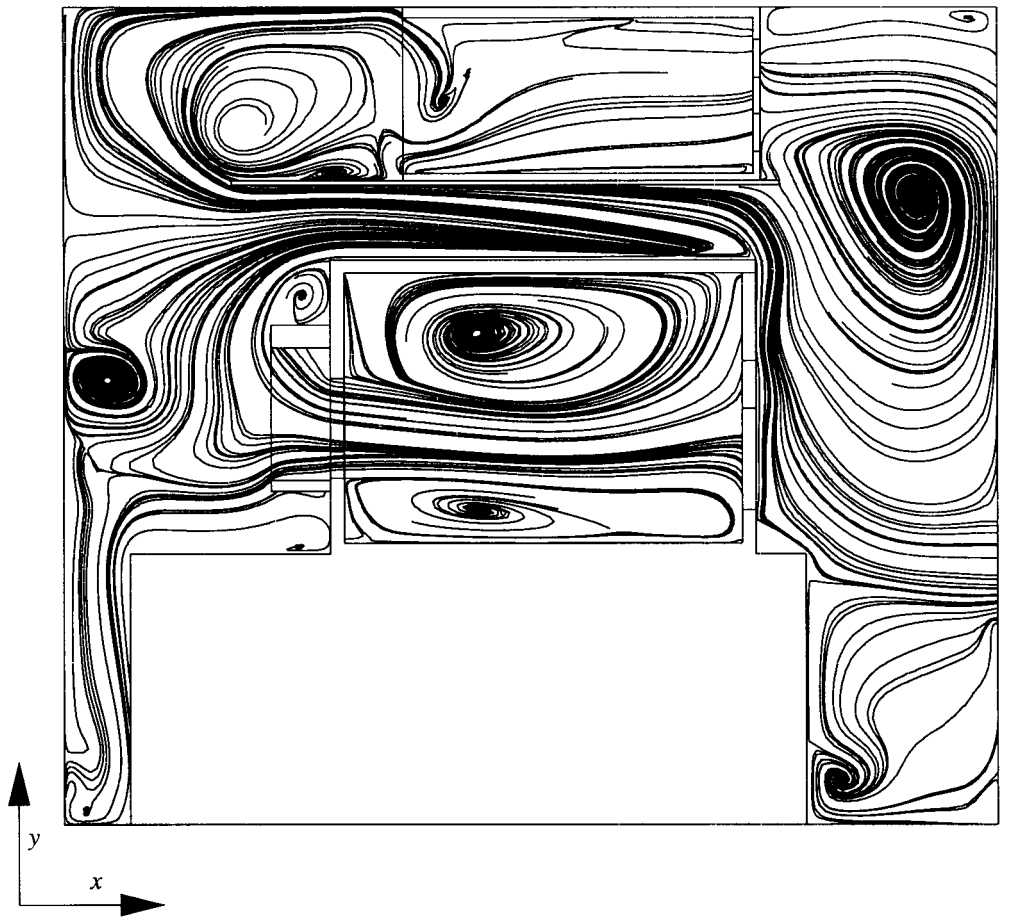

Figure 6. Instantaneous streamline plots for the zonal $k-\varepsilon/k-l$ model: (a) mid $x-y$ plane; (b) mid $x-z$ plane.

3.4. Spatial velocity variations

Comparisons are made with measurements along lines/profiles 1–6 shown in Figure 7. Table II gives the exact profile locations. Figure 8 compares k–ε/k–l_2 model velocity predictions with time averaged measurements. Velocities are normalized by the approximate average fan axial velocities ($U_0 \approx 4.5$ m s^{-1}). The addition symbols and circles represent Pitot static tube and

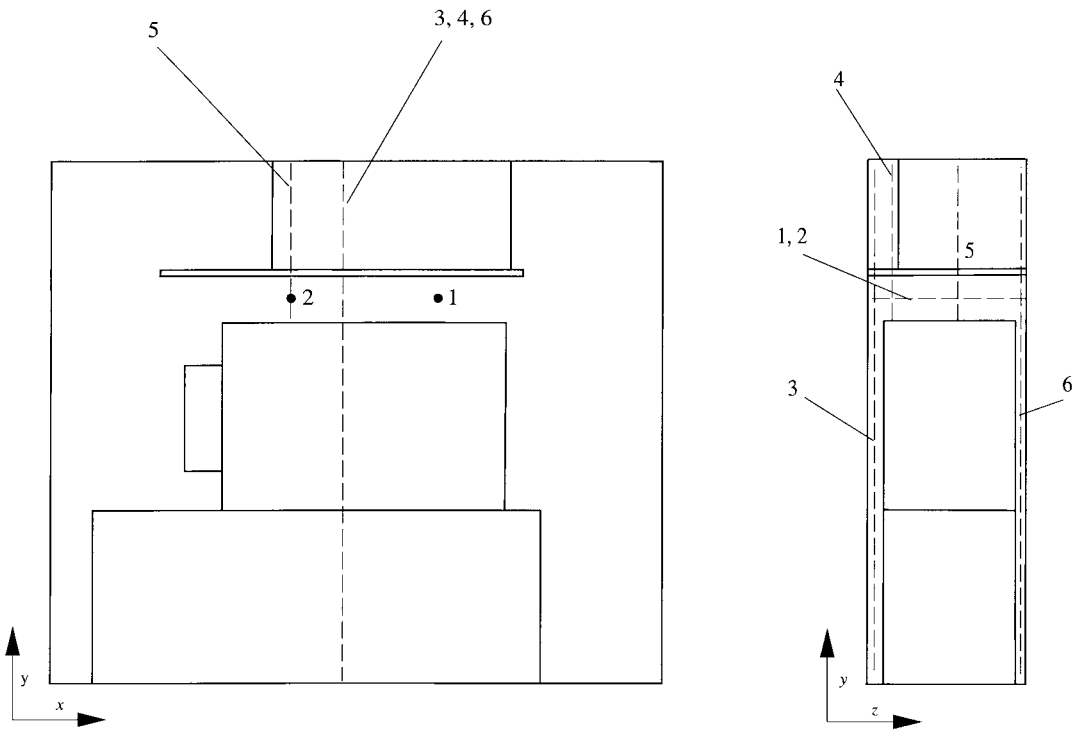

Figure 7. Schematic diagram showing positions for velocity and turbulence intensity profiles.

Table II. Profile locations.

Profile	X	Y	Z
1	0.533	0.734	—
2	0.373	0.734	—
3	0.413	—	0.060
4	0.413	—	0.100
5	0.373	—	0.575
6	0.413	—	0.962
7	0.373	0.914	—

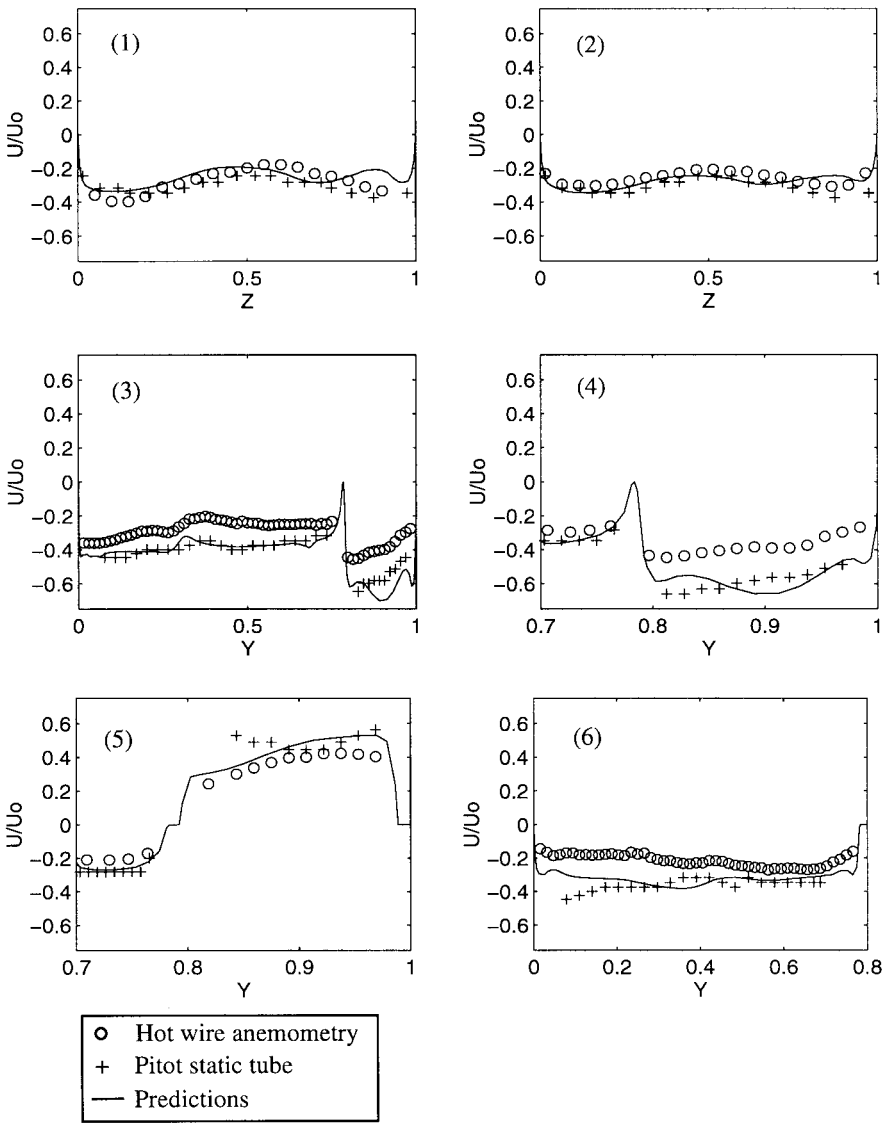

Figure 8. Comparison of k–ε/k–l_2 velocity predictions with measurements.

hot wire anemometry measurements respectively. The line represents the predictions. The Pitot static tube measurements give higher velocities than the hot wire. Due to an area reduction effect, this is partly to be expected [40], however, not to the extent shown. Generally, velocities are low (around 2 m s^{-1}). This makes hot wire calibration difficult and buoyancy related errors significant.

Also, pressure differences across the Pitot static tube are small and so difficult to accurately measure. Importantly, the probe position is located by crude visual alignment. Consequently, measurements have around a ± 25 per cent error. This figure is backed up by the large differences between the Pitot static and hot wire measurements in some regions.

Considering the experimental and also modelling uncertainties, agreement in Figure 8 is reasonable. For all models, predictions are closest to the Pitot static tube measurements. It is likely that these (which are not subjected to a calibration error) are the more accurate. For all nine turbulence models, velocity plots are similar. Therefore, rather than present numerous plots, the percentage error for each model is summarized in Table III. The errors are based on Equation (37) and averages of the Pitot static and hot wire data. Tabulated errors are nearly 3 per cent less for the Pitot static tube data. The average discrepancy for all models is similar between 18 and 23 per cent, and within the experimental error. The significant measurement errors make it difficult to draw firm conclusions regarding the relative accuracies of the models. However, the results they give are similar, suggesting for some engineering applications, *ml* models could be adequate.

Interestingly, based on the Pitot static tube data, the least and most accurate models are the ml_1, k–ε (both having a 21 per cent error) and k–ε/k–l_2, k–ε/ml_2 models (both these zonal models have a 14 per cent error) respectively.

3.5. Temporal velocity variations

Temporal velocity variations are considered for six points on profiles 1–6. Points 1 and 2 are located at $Z = 0.55$, and points 3–6 are at $X = 0.30$, 0.91, 0.91 and 0.30 respectively. Measurements show there are two dominant unsteady flow component frequencies of about 0.5 and 0.75 Hz. The average amplitude for these is about 0.25 m s^{-1}.

Figure 9 shows velocity time traces for point 1 and the k–l_1 model. Figure 9(a) is for the first order upwind scheme, U velocity component. Figure 9(b)–(d) give the CONDIF scheme for U, V and W components respectively. For points 1–6, the frequencies of the dominant unsteady CONDIF flow components are all 0.12 Hz (around four times lower than the measured average). The velocity amplitudes at these points vary considerably, averaging 0.16 m s^{-1} (approximately 1.5 times lower than the measured average). The diffusive upwind scheme's trace is steady, illustrating a danger of its use.

Table III. Summary of percentage velocity errors for each profile and model.

Model	1	2	3	4	5	6	Average
(I) ml_1	33	23	26	27	18	14	23
(II) l–v	26	15	30	24	17	15	21
(III) k–l_1	25	18	26	23	18	17	21
(IV) k–l_2	26	21	25	34	15	17	23
(V) k–ε	20	14	16	20	20	23	19
(VI) k–ε/k–l_2	20	13	20	20	11	19	17
(VII) k–ε/ml_1	16	8	26	24	14	29	19
(VIII) k–ε/ml_2	14	12	22	23	12	28	18
(IX) nl–k–l_1	27	20	24	18	15	19	20

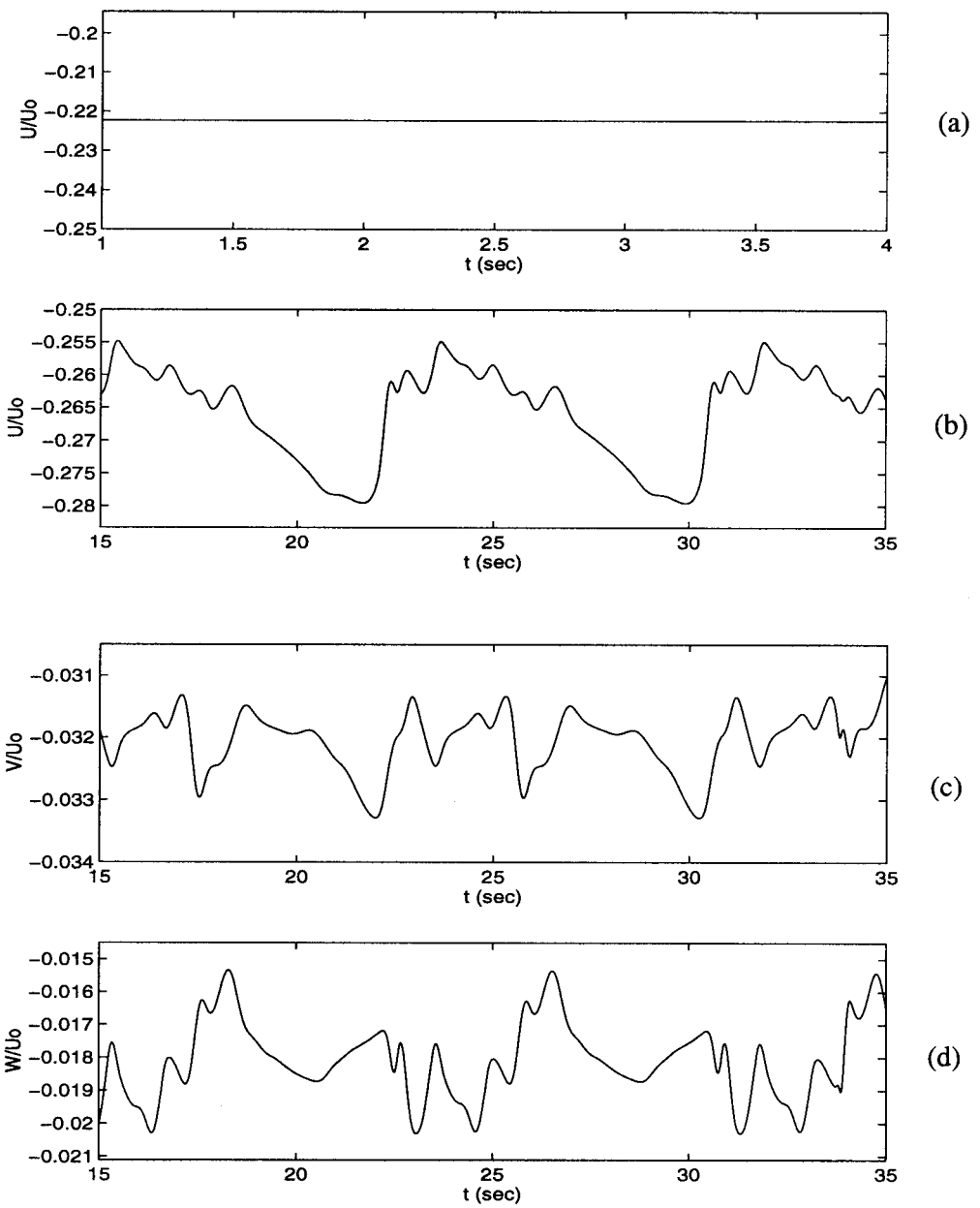

Figure 9. Variation of fluid flow with time at point 1 for the k–l_1 model: (a) first order upwind scheme U velocity component, (b) CONDIF scheme U velocity component, (c) CONDIF scheme V velocity component, (d) CONDIF scheme W velocity component.

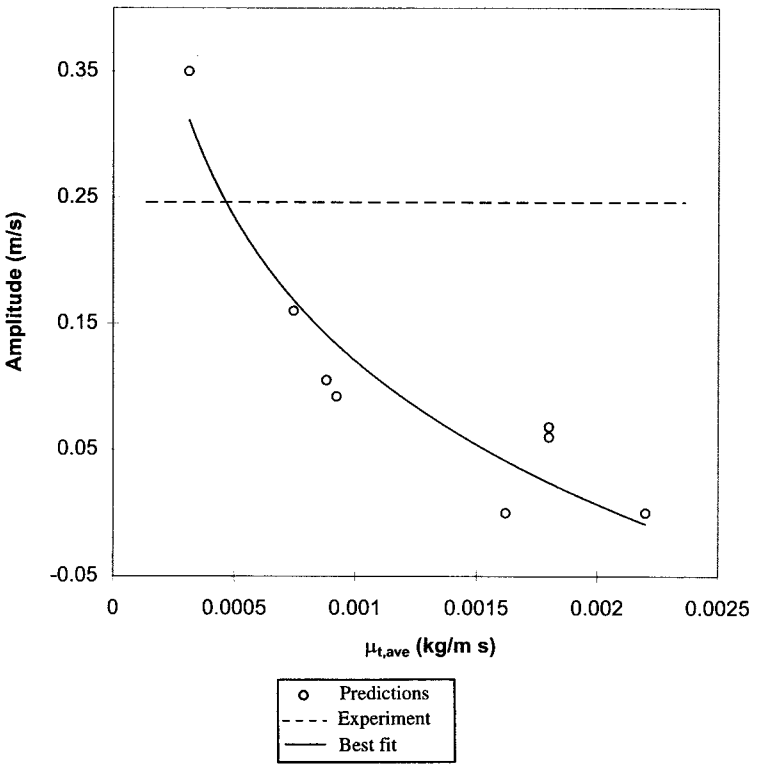

Figure 10. Plot of amplitude against turbulent viscosity.

Figure 10 is a plot of averaged predicted amplitude against turbulent viscosity for different turbulence models. Symbols represent the predictions and the full line a best fit to these. The horizontal dashed line gives the measured average amplitude. Some nl–k–l_1 model, momentum equation, Reynolds stress components are not incorporated through diffusion terms and so this data point is excluded. As can be seen, amplitudes vary significantly, decreasing with increasing μ_t. This is consistent somewhat with the observation of Brackenridge [4]. Zero amplitude points correspond to the k–ε and k–ε/k–l_2 models. As will be seen later, for these k and μ_t are overestimated. The predicted dominant wave frequencies vary significantly (0–3.33 Hz), generally decreasing with μ_t.

3.6. Spatial turbulence intensity variations

Figure 11 compares time averaged turbulence intensity predictions (T_i) with measurements. The dotted, full and dashed lines are for the nl–k–l_1, k–ε/k–l_2 and k–ε models respectively. The nl–k–l_1 and k–ε computations give the T_i extremes for all the models. Unlike for velocities, the models give significantly different intensities. The nl–k–l_1 values are lower than

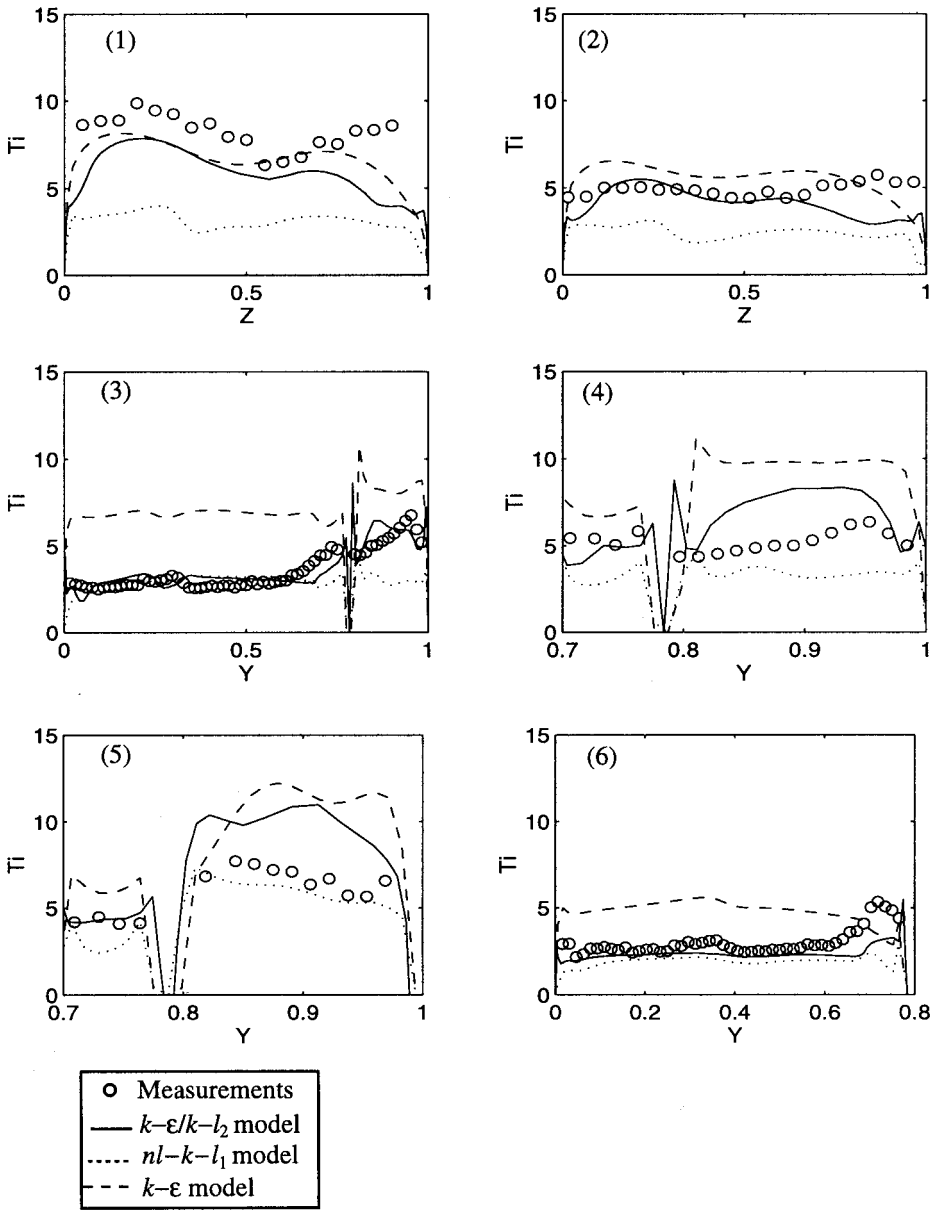

Figure 11. Comparison of turbulence intensity predictions with measurements.

Table IV. Summary of percentage error in T_i for each profile and model.

Model	1	2	3	4	5	6	Average
(III) k–l_1	−62	−51	−26	−32	−20	−39	−38
(IV) k–l_2	−53	−41	−22	−28	−27	−29	−33
(V) k–ε	−18	25	107	73	68	72	60
(VI) k–ε/k–l_2	−28	−25	18	37	37	−27	29
(VII) k–ε/ml_1	−18	34	—	40	41	—	33
(VIII) k–ε/ml_2	−15	40	—	43	41	—	35
(IX) nl–k–l_1	−62	−52	−29	−37	−23	−43	−41

those for the k–ε model. The zonal predictions tend to lie between the above two extremes. The measured intensities include a contribution due to flow unsteadiness. Despite this discrepancy, which makes the measurements too high, comparison is worthwhile. For example, the graphs certainly show the standard k–ε model overpredicts intensities.

As with velocities, rather than present many curves and graphs, percentage errors for all models are summarized in Table IV. A sign has been given to each error, indicating if the predictions are on average too high or low. The sign is attached after the error has been evaluated. For the error in the last column, it is based on the sign of the sum of the preceding values. Blanks are where *ml* models are used.

The table shows the two equation solutions tend to overpredict intensities. Of these, clearly the k–ε model is the worst, with a 60 per cent average error. Tests for a channel region, corresponding to profiles 1 and 2, show that wall functions are partly the cause of this. As first off wall grid node positions vary from $y^+ = 30$ to 0.1, k–ε intensities increase by around 20 per cent (the k–l_1 model is far less sensitive). As noted earlier, for the flows here, it is difficult to ensure $y^+ > 30$ everywhere. However, to a lesser extent, even the zonal two-equation models' intensities are high. A further reason for the magnitude overprediction could be stagnation effects (see, for example, Kato and Launder [41] and Iacovides *et al.* [42]). Importantly, the lowest average intensities are for the nl–k–l_1 model, which accounts for anisotropy. Therefore, these results suggest non-linear two-equation models may give improvements. The Yap [43] correction to ε prevents excessively high near-wall turbulence in separated flows. This may also give further improvements.

The table shows the k–l models tend to give lower intensities. (Interestingly, the first order upwind scheme significantly lowers these values further.) The constrained dissipation scale may excessively limit T_i. But, without further analysis, to account for the unsteady component, this is not clear. To check this idea, computations are corrected, adding the unsteady flow components to intensities.

3.7. Stochastic turbulence intensity correction procedure

Using Equations (29) and (30) to combine predicted time traces with intensities enables direct T_i comparisons. These are shown in Table V.

The k–ε, k–ε/k–l_2 and nl–k–l_1 models give steady flows and so are not shown. Unlike the k–l results, the predicted k–ε/ml intensities are relatively high and unsteadiness amplitudes

Table V. Corrected T_i predictions.

Model	1	2	3	4	5	6
(III) k–l_1	−60	−49	26	45	31	−37
(IV) k–l_2	−51	−37	34	−27	−27	−25
(VII) k–ε/ml_1	−18	34	—	40	42	—
(VIII) k–ε/ml_2	−15	40	—	44	42	—

low. Therefore, the correction procedure makes little difference to k–ε/ml intensities (see Tables IV and V). For the k–l models, corrected intensity levels are significantly increased. However, the overall agreement is not improved and for the k–l_2 model, values are still too low. Importantly, using higher amplitudes from measured traces in the stochastic procedure still suggests the k–l model has a tendency to slightly underpredict T_i.

4. CONCLUSIONS

The economical prediction of turbulent oscillatory flow at transitional Reynolds numbers was considered for an enclosure representative of an idealized electronics system. To assess the accuracy of numerical models, comparison was made with Pitot static tube and hot wire anemometry data. Although the flow is unsteady, turbulence intensity measurements are not phase averaged. The effect of this on comparisons was assessed by stochastically correcting predictions.

Normal wall distances, required in some turbulence models, were evaluated using a modified Poisson equation-based technique. Solution of the Poisson and fluid flow equations were accelerated using multi-level schemes. These gave valuable computer time savings. The Poisson equation-based wall distance technique was shown to be effective.

The following turbulence models were tested: (I) a standard mixing length model (ml_1); (II) a single-equation law of the wall based l–v model; (III) a high-Reynolds number k–l_1 model; (IV) a low-Reynolds number k–l_2 model; (V) the standard k–ε model; (VI) a zonal method using the k–ε model away from walls ($y^+ \geq 60$) and the k–l_2 model near walls (k–ε/k–l_2); (VII) a zonal model combining the k–ε and ml_1 models (k–ε/ml_1); (VIII) model VII with a modified damping function (k–ε/ml_2), and (IX) a high-Reynolds number non-linear eddy viscosity model (nl–k–l_1). For this, velocities used in non-linear turbulence terms were smoothed using the restriction operators of the multi-level algorithm.

Predicted velocities for all models were similar and mostly within the experimental error. Results suggest zero-equation models may be acceptable for some engineering applications. Based on the perhaps more reliable Pitot static tube velocity data, the least and most accurate models were the ml_1, k–ε (both having a 21 per cent error) and the k–ε/k–l_2, k–ε/ml_2 models (both these zonal models having a 14 per cent error) respectively.

The predicted temporal velocity variations for the different turbulence models varied significantly, none comparing with measurements. Computed unsteadiness amplitudes decreased with increasing turbulent viscosity. Importantly, for the diffusive first order upwind scheme, there was no detectable unsteadiness, illustrating a danger of using it.

Predictions showed areas of significant streamline curvature and several vortex structures. Unlike for velocities, the models gave significantly different turbulence intensities (T_i). The two-equation models tended to overpredict intensities and the one-equation models tended to underpredict them. The $k-\varepsilon$ model had the worst intensity accuracy with an average error of 60 per cent. The zonal turbulence models showed promise; the $nl-k-l_1$ results suggesting their tendency to overpredict T_i could be reduced if anisotropy is accounted for. More accurate data is required to draw firm conclusions.

ACKNOWLEDGMENTS

A grid independence computation was performed on the Engineering and Physical Sciences Research Council's (EPSRC) DEC Super Scalar machine at the Rutherford Appleton laboratory. The author is also grateful to acknowledge the support of the EPSRC (grant number GR/L05600), NCR (Scotland) Ltd, Hewlett Packard Ltd, Digital Equipment Ltd and GEC Marconi Avionics. He would like to express his thanks to Drs Hector Iacovides and Masoud Rokni for their countless helpful discussions relating to the implementation of the turbulence models used here. Thanks are also due to Dr Zhiqiu Pan for the helpful discussions had on some technical issues relating to this work.

REFERENCES

1. Tucker PG. CFD applied to electronic systems: a review. *Transactions of the IEEE CPMTA* 1997; **20**(4): 518–529.
2. Rockwell D. Prediction of oscillation frequencies for unstable flow past cavities. *Transactions of the ASME, Journal of Fluids Engineering* 1977; **June**: 294–300.
3. Rockwell D, Naudascher E. Self sustained oscillations of impinging free shear layers. *Annual Reviews in Fluid Mechanics* 1979; **11**: 67–94.
4. Brackenridge JB. Transverse oscillations of a liquid jet. *Journal of the Acoustical Society of America* 1960; **32**(10): 1237–1242.
5. Ghaddar NK, Korczak KZ, Mikic BB, Patera AT. Numerical investigation of incompressible flow in grooved channels. Part 1. Stability and self-sustained oscillations. *Journal of Fluid Mechanics* 1986; **163**: 99–127.
6. Ghaddar NK, Magen M, Mikic BB, Patera AT. Numerical investigation of incompressible flow in grooved channels. Part 2. Resonance and oscillatory heat-transfer enhancement. *Journal of Fluid Mechanics* 1986; **168**: 541–567.
7. Patera AT, Mikic BB. Exploiting hydrodynamic instabilities. Resonant heat transfer enhancement. *International Journal of Heat Mass Transfer* 1986; **29**(8): 1127–1138.
8. Nigen JS, Amon CH. Time-dependent conjugate heat transfer characteristics of self-sustained oscillatory flows in a grooved channel. *ASME Journal of Fluids Engineering* 1994; **116**: 499–507.
9. Amon CH. Spectral element-Fourier method for unsteady conjugate heat transfer in complex geometry flows. *Journal of Thermophysics and Heat Transfer* 1995; **9**(2): 247–253.
10. Nigen JS, Amon CH. Effect of Material composition and localised heat generation on time dependent conjugate heat transport. *International Journal of Heat Mass Transfer* 1995; **38**(9): 1565–1576.
11. Pulicani JP, Crespo Del Arco E, Randriamampianina A, Bontoux P, Peyret R. Spectral simulations of oscillatory convection at low Prandtl numbers. *International Journal for Numerical Methods in Fluids* 1990; **10**: 481–517.
12. Rockwell D. Vortex body interactions. *Annual Reviews in Fluid Mechanics* 1998; **30**: 199–229.
13. Kuay ST. Study of fluid flow and particle transport in mechatronic systems. MPhil Thesis, University of Dundee, 1999.
14. Spalding DB. Calculation of turbulent heat transfer in cluttered spaces. Unpublished paper presented at the *10th International Heat Transfer Conference*, Brighton, U.K., 1994.
15. *Spalding DB. A single formula for the law of the wall. Transactions of the ASME Series A, Journal of Applied Mechanics* 1961; **28**(3): 444–458.
16. Wolfshtein M. The velocity and temperature distribution in one-dimensional flow with turbulence augmentation and pressure gradient. *International Journal of Heat Mass Transfer* 1969; **12**: 301–318.
17. Launder BE, Spalding DB. The numerical computation of turbulent flows. *Computer Methods in Applied Mechanical Engineering* 1974; **3**: 269–289.

18. Speziale CG. On non-linear $k-l$ and $k-\varepsilon$ models of turbulence. *Journal of Fluid Mechanics* 1987; **178**: 459–475.
19. Iacovides H, Theofanopoulos IP. Turbulence modelling of axisymmetric flow inside rotating cavities. *International Journal of Heat and Fluid Flow* 1991; **12**(1): 2–11.
20. Iacovides H, Chew JW. The computation of convective heat transfer in rotating cavities. *International Journal of Heat and Fluid Flow* 1993; **14**(2): 146–154.
21. Tucker PG. Assessment of geometric multilevel convergence and a wall distance method for flows with multiple internal boundaries. *Applied Mathematical Modelling* 1998; **22**: 293–311.
22. Sethian JA. Fast marching methods. *SIAM Review* 1999; **41**(2): 199–235.
23. Koosinlin ML, Launder BE, Sharma BI. Prediction of momentum, heat and mass transfer in swirling turbulent boundary layers. *Transactions of the ASME*, *Journal of Heat Transfer* 1974; **May**: 204–209.
24. Patankar SV. *Numerical Heat Transfer and Fluid Flow*. Hemisphere: New York, 1980.
25. Runchal AK. CONDIF: a modified central-difference scheme for convective flows. *International Journal for Numerical Methods in Engineering* 1987; **24**: 1593–1608.
26. Patankar SV, Spalding DB. A calculation procedure for heat mass and momentum transfer in three-dimensional parabolic flows. *International Journal of Heat and Mass Transfer* 1972; **15**: 1787–1806.
27. Brandt A. Multi-level adaptive solutions to boundary-value problems. *Mathematics of Computation* 1977; **31**(138): 333–390.
28. Lonsdale G. Solution of a rotating Navier–Stokes problem by a non-linear multigrid algorithm. *Journal of Computational Physics* 1988; **79**: 177–190.
29. Vaughan CM, Gilham S, Chew JW. Numerical solutions of rotating disc flows using a non-linear multigrid algorithm. In *Proceedings of the 6th International Conference on Numerical Methods in Laminar and Turbulent Flow*, Taylor C (ed.). Pineridge Press: Swansea, U.K., 1989; 63–67.
30. Rayner D. Multigrid flow solutions in complex two dimensional geometries. *International Journal for Numerical Methods in Fluids* 1991; **20**: 61–80.
31. Rayner D. A numerical study into the heat transfer beneath the stator blade of an axial compressor. PhD thesis, School of Engineering, The University of Sussex, Falmer, Brighton, 1990.
32. Shyy W, Chen M. Pressure based multigrid algorithm for flow at all speeds. *AIAA Journal* 1992; **30**(11): 2660–2669.
33. Shyy W, Sun C, Chen M, Chang KC. Multigrid computation for turbulent recirculating flows in complex geometries. *Numerical Heat Transfer* 1993; **A23**: 79–98.
34. Thompson MC, Ferziger JH. An adaptive multigrid technique for the incompressible Navier–Stokes equations. *Journal of Computational Physics* 1989; **82**: 94–121.
35. Raw M. A coupled algebraic multi-grid method for the 3D Navier–Stokes equations. In *Notes on Numerical Fluid Mechanics: Fast Solvers for Flow Problems*, vol. 49, Hackbusch W, Wittum G (eds). Vieweg: Wiesbaden, 1995; 204–215.
36. Ruge J, Stuben K. Algebraic multigrid. *Arbeitspapiere der GMD* 1986; Paper number **210**.
37. Tucker PG. Numerical and experimental work on rotating cavities. Technical Report 90/TFMRC/TN91, Thermo-Fluid Mechanics Research Centre, School of Engineering and Applied Sciences, University of Sussex, Falmer, Brighton, 1990.
38. Gosman AD, Ioannides E. Aspects of computer simulation of liquid fuelled combustors. *Journal of Energy* 1983; **7**: 482–490.
39. Fried E, Idelchik IE. *Flow Resistance: A Design Guide for Engineers*. Hemisphere: New York, 1989.
40. Kim JJ. Investigation of separation and reattachment of turbulence shear layer: flow over a backward facing step. PhD thesis, University of Stanford, 1978.
41. Kato M, Launder BE. The modelling of turbulent flow around stationary and vibrating square cylinders. In *Proceedings of the 9th Symposium on Turbulent Shear Flows*, *Kyoto*, *Japan*, 1993; 10-4-1–10-4-6.
42. Iacovides H, Leschziner MA, Li H-Y. Computation of axisymmetric rotor-stator flows related to cooling passages of electrical generators. In *Proceedings of the 10th International Conference on Numerical Methods in Laminar and Turbulent Flow*, *Swansea*, Taylor C, Cross J (eds). Pineridge Press: Swansea, U.K., 1977; 977–988.
43. Yap CR. Turbulent heat and momentum transfer in recirculating impinging flows. PhD thesis, Department of Mechanical Engineering, Faculty of Technology, University of Manchester, 1987.

